PNAS RESEARCH ARTICLE | CHEMISTRY

Ordered heterogeneity of molecular photosensitizer toward enhanced photocatalysis

Ji-Hong Zhang[a,1], Yun-Nan Gong[a,1], Hong-Juan Wang[a,1], Yu-Chen Wang[a], Wei Yang[a], Jian-Hua Mei[a], Di-Chang Zhong[a,2], and Tong-Bu Lu[a,2]

Edited by Alexis Bell, University of California, Berkeley, CA; received October 5, 2021; accepted December 22, 2021

Ordered heterogeneity is significant for molecular photosensitizers to enhance their practical applications. However, the ordered heterogeneity of molecular photosensitizers is still a great challenge. In this article, we describe a supramolecular assembly method for the heterogeneity of molecular photosensitizers, with which a mononuclear Zn(II) molecular photosensitizer in solution was orderly assembled in long range via π–π stacking interactions, affording a cheap, solid photocatalyst (π-1) with a porous structure. With Co(II), Fe(III), or Ni(II) as a cocatalyst, π-1 shows noticeably better photocatalytic activity for CO_2 reduction than in a homogeneous system. The definite crystal structure and precise position of the catalytic center in π-1 were determined by single-crystal X-ray diffraction combined with X-ray diffraction adsorption spectra, based on which the enhanced activity of π-1 for photocatalytic CO_2 reduction was revealed by theoretical calculation. Thus, the reduced energy gap after ordered heterogeneity accelerates the electron transfer, greatly boosting the photocatalytic CO_2 reduction activity. This work demonstrates a method for developing crystalline, heterogeneous photocatalysts with definite structures and enhanced, catalytic performance.

molecular catalysis | homogeneous catalysis | heterogeneous catalysis | heterogeneity | photocatalytic CO_2 reduction

Photocatalysis has shown promising applications in fields of energy, environment, biology, and so on (1–6). In heterogeneous photocatalytic systems, semiconductors are indispensable, which absorb photons with energy equal to or greater than their band gaps to generate electron–hole pairs for subsequent reduction or oxidation reactions (7–13). Typical semiconductors, including inorganic quantum dots such as CdS and organic polymers such as C_3N_4, have no definite crystal structures, which hinders the exact revealing of performance–structure correlation and catalysis mechanism (14–16). In homogeneous photocatalytic systems, molecular catalysts and photosensitizers have well-defined structures beneficial for catalysis mechanism revealing and helpful for further structural design and performance optimization (17–23). However, photosensitizers mostly used in homogeneous photocatalytic systems are Ru/Ir noble–metal complexes (24–27), and the separation and recycling of them is a big problem. The heterogeneity of molecular photosensitizers could enhance their separation and recycling capability, which is conventionally achieved by loading them into/on two/three-dimensional supports through covalent bonds, electrostatic interactions, and supramolecular interactions (28–32). Nonetheless, the structures of the resulting composites are unclear. Thus, the development of highly crystalline heterogeneity methods for molecular photosensitizers, albeit greatly challenging, is meaningful and desirable, with which heterogeneous photosensitizers with excellent performance, well-defined structures, and definite catalysis mechanisms would be expected.

Since 2011, noncovalent interactions have been found suitable forces accessible to build stable, porous supramolecular frameworks besides covalent/coordination bonds. Typical examples are a number of hydrogen-bonded organic frameworks reported recently (33–37). The successful construction of these ordered, porous materials inspires us to achieve highly crystalline heterogeneity of molecular photosensitizers by supramolecular assembly. As the supramolecular assembly process neither destroys the structures of molecular photosensitizers nor affects the coordination environment of the metal centers, a highly ordered, solid photocatalyst, in which high-density molecular photosensitizers are periodically dispersed, may be obtained. As a proof of concept research, we found that **π-1**, the first example of porous supramolecular π frameworks, could serve as a model. **π-1** is assembled from mononuclear [Zn(phen)$_2$L] complex units [H_2L = 1-(4-carboxyphenyl)-5-mercapto-1H-tetrazole; phen = 1,10-phenanthroline monohydrate] only by intermolecular π–π stacking interactions (38), which shows good thermal and chemical stability in aqueous solution and common organic solvents, thus, facilitates the heterogeneous photocatalysis studies. In addition, mononuclear [Zn(phen)$_2$L] complex units can be easily formed by combining Zn(II) with H_2L and

Significance

The photosensitizer is one of the important components in the photocatalytic system. Molecular photosensitizers have well-defined structures, which is beneficial in revealing the catalysis mechanism and helpful for further structural design and performance optimization. However, separation and recycling of the molecular photosensitizers is a great problem. Loading them into/on two/three-dimensional supports through covalent bonds, electrostatic interactions, and supramolecular interactions is a method that enhances their separation and recycling capability. Nonetheless, the structures of the resulting composites are unclear. Thus, the development of highly crystalline heterogeneity methods for molecular photosensitizers, albeit greatly challenging, is meaningful and desirable in photocatalysis, through which heterogeneous photosensitizers with well-defined structures, definite catalysis mechanisms, and good catalytic performance would be expected.

Author contributions: D.-C.Z. and T.-B.L. designed research; J.-H.Z., Y.-C.W., W.Y., and J.-H.M. performed research; H.-J.W. performed theoretical calculations; Y.-N.G., H.-J.W., D.-C.Z., and T.-B.L. analyzed data; and D.-C.Z. wrote the paper.

The authors declare no competing interest.

This article is a PNAS Direct Submission.

[1] J.-H.Z., Y.-N.G., and H.-J.W. contributed equally to this work.

[2] To whom correspondence may be addressed. Email: dczhong@email.tjut.edu.cn or lutongbu@tjut.edu.cn.

This article contains supporting information online at http://www.pnas.org/lookup/suppl/doi:10.1073/pnas.2118278119/-/DCSupplemental.

phen in *N*,*N*-dimethylformamide (DMF), which helps construct a homogeneous photocatalytic system in which [Zn(phen)$_2$L] complex unit serves as a molecular photosensitizer. These features provide a chance to prove the above concept.

As a result, we found that the photocatalytic performance of the above mononuclear Zn(II) molecular complex could be greatly enhanced after ordered heterogeneity through π–π stacking. The resulting crystalline orderly photocatalyst of **π-1**, after anchoring with Co(II), Fe(III), or Ni(II) as a cocatalyst, shows noticeably better photocatalytic performance for CO_2 reduction than it in the homogeneous system in the absence of additional photosensitizer (Scheme 1). The CO evolution rate reaches as high as 494.4 $\mu mol \cdot g^{-1} \cdot h^{-1}$ and selectivity to CO as high as 100%. The enhanced catalytic performance of **π-1** can be ascribed to the higher stability and the reduced energy gap structure after ordered heterogeneity.

Results

Synthesis and Structure. The monomer Zn(II) complex unit [Zn(phen)$_2$L] can be easily formed by reacting $Zn(Ac)_2 \cdot 2H_2O$, H_2L, and phen in DMF in a molar ratio of 1:1:2. Electrospray ionization mass spectrometry confirm the successful formation of [Zn(phen)$_2$L] in the solution (*SI Appendix*, Fig. S1). Ultraviolet-visible (UV-vis) spectra show that [Zn(phen)$_2$L] in DMF exhibits strong UV adsorption, with the adsorption peaks at 268 and 335 nm (*SI Appendix*, Fig. S2).

Diffusing diethyl ether into the DMF solution of [Zn(phen)$_2$L], large amount of yellow microcrystals were obtained. Powder X-ray diffraction (XRD) analysis revealed that the structure of these microcrystals is the same as **π-1** prepared under solvothermal conditions (*SI Appendix*, Fig. S3) (38). Scanning electron microscope (SEM) measurements further confirmed the similar, rod-like morphology (Fig. 1).

Considering the pores of **π-1** are richly decorated with free-standing thiolate groups (*SI Appendix*, Fig. S4), we tried to anchor catalytically active M [M = Co(II), Fe(III), Ni(II)] onto the pore surface of **π-1** by coordination interaction. Thus, a simple impregnation approach was used to incorporate M into **π-1**, resulting in three types of crystalline **π-1-M** heterogeneous photocatalysts. Remarkable color changes preliminarily illustrate the incorporation of M into **π-1** (*SI Appendix*, Fig. S5). Inductively coupled plasma mass spectrometer (ICP-MS) tests further confirm the successful incorporation of Co/Fe/Ni into **π-1** (*SI Appendix*, Fig. S6 and Table S1). Powder XRD studies show that the patterns of **π-1-M** are identical to those of **π-1**, demonstrating that the framework of **π-1** keeps stable after introduction of M (*SI Appendix*, Fig. S7). SEM images show that **π-1-M** assume rod-like morphology, the same as **π-1** (Fig. 1), also illustrating that **π-1** can keep stable after bonding with M. The element-mapping images show that there are C, N, O, S, and Zn in **π-1**, and the introduced Co/Fe/Ni is highly dispersed in inner and outer **π-1** (*SI Appendix*, Fig. S8). These observations indicate that the Co/Fe/Ni has been successfully anchored into **π-1**, and the bonding sites for Co/Fe/Ni in **π-1** are homogeneous. The Fourier transform infrared spectra (FT-IR) measurements showed that the characteristic bands of the carboxylic groups in **π-1** appear at 1,604 and 1,540 cm^{-1}, and the intensity of these bands slightly increases in **π-1-M** (*SI Appendix*, Fig. S9*A*). These observations indicate that there is bonding interaction between the carboxylic group and Co/Fe/Ni, and the carboxyl group employs a bridge–chelate coordination mode to bond with Co/Fe/Ni (39, 40). Moreover, new adsorption peaks at ∼417 cm^{-1}, corresponding to the stretch/bending vibration of S–M bond (41), appear for **π-1-M** (*SI Appendix*, Fig. S9*B*), suggesting that, besides carboxylic groups, the thiolate groups are also the bond sites for Co/Fe/Ni within **π-1**.

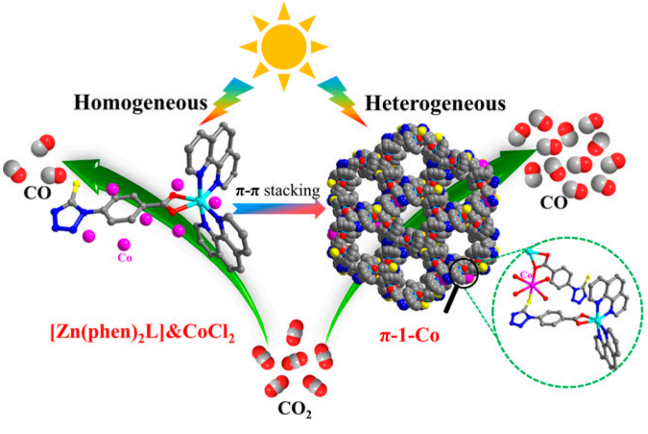

Scheme 1. Schematic illustration for photocatalytic CO_2 reduction based on homogeneous ([Zn(phen)$_2$L]) and heterogeneous (**π-1**) photocatalyst, in which **π-1** is formed by heterogeneity of molecular photosensitizer [Zn(phen)$_2$L] via π–π stacking interactions.

X-ray photoelectron spectroscopic (XPS) measurements were performed to further identify the chemical composition and valence states of **π-1-M**. The results show that the binding energy peaks for Co $2p_{1/2}$ and Co $2p_{3/2}$ appear at 796.3 and 780.4 eV, respectively; those for Fe $2p_{1/2}$ and Fe $2p_{3/2}$ at 724.4 and 711.1 eV, respectively; and those for Ni $2p_{1/2}$ and Ni $2p_{3/2}$ at 873.1 and 855.5 eV, respectively (*SI Appendix*, Fig. S10). These observations illustrate that the oxidation valences of Co/Fe/Ni in **π-1-M** have not changed during the anchoring process (42–44). In the high-resolution S 2p spectra of **π-1** (*SI Appendix*, Fig. S11*A*), the peaks at 161.0 and 162.2 eV correspond to the binding energies of S $2p_{3/2}$ and S $2p_{1/2}$, respectively. The peak at 167.7 eV is assigned to the satellite peak. In contrast to **π-1**, the S 2p XPS spectra of **π-1-M** show broad peaks at ∼162.3 eV (*SI Appendix*, Fig. S11 *B–D*), demonstrating the bonding of thiolate groups with M and the anchoring of M really via the coordination of thiolate groups (45). Additionally, the high-resolution O 1s spectra of **π-1** show three peaks, corresponding to the M–O (∼530.4 eV), M–OH (∼531.2 eV), and physisorption/chemisorption of oxygen (∼532.4 eV) at/near the surface (*SI Appendix*, Fig. S12*A*) (46). Compared with **π-1**, slight shifts to higher-binding energy of M–O are observed in **π-1-M**, which indicate that the O atoms of the carboxylic groups participate in the coordination with M. Moreover, the intensity of the peaks corresponding to the M–O in **π-1-M** obviously become stronger (*SI Appendix*, Fig. S12 *B–D*), which further indicates that the contents of O species coordinating with M increase. These results, coupled with that of the FT-IR discussed in *Synthesis and Structure*, illustrate that M are anchored on **π-1** via S–M and O–M coordination interactions (46).

X-ray absorption spectra were further measured to reveal the electronic structure and coordination environment of M in **π-1-M**. Taking **π-1-Co** as a representative, the X-ray absorption near-edge structure analyses shows that the absorption edge of **π-1-Co** is similar to that of CoO, which suggests that the valence state of Co in **π-1-Co** is +2, consistent with the result of XPS (Fig. 2*A*). Extended X-ray absorption fine structure (EXAFS) analyses shows that, for Co foil, the main peak at

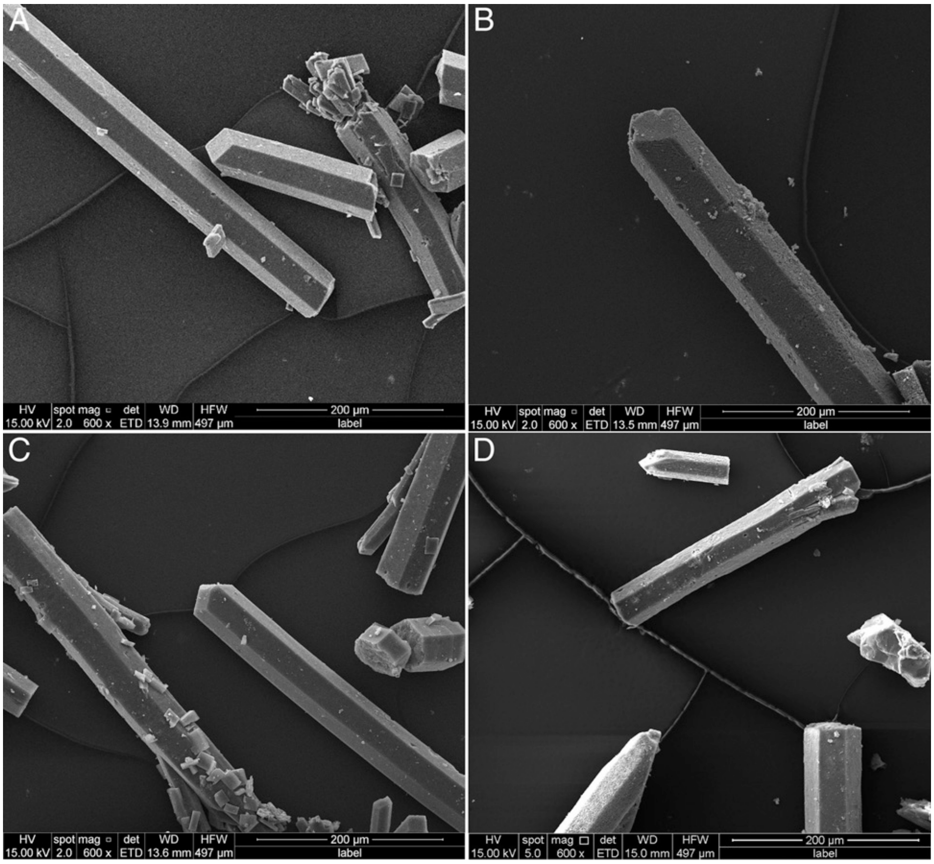

Fig. 1. SEM images for **π-1** (*A*), **π-1-Co** (*B*), **π-1-Fe** (*C*), and **π-1-Ni** (*D*) (HV: high voltage, WD: work distance, HFW: horizontal field width, and ETD: Everhart–Thornley detector).

2.20 Å corresponds to the scattering path of Co–Co. For **π-1-Co**, the main peak displays around 1.66 Å, which is assigned to the Co–O or Co–S bonds. No peak corresponding to the Co–Co bond is detected, indicating that the Co is atomically dispersed (Fig. 2*B*). This conclusion is further confirmed by wavelet transform contour plots. As shown in Fig. 2*C*, by comparison with those of CoO, CoS, and Co foil, two prominent features centered at k space of ~6.5 and 4.0 $Å^{-1}$ are observed, which can be assigned to S–Co and O–Co bonds, respectively. These observations not only verify the absence of Co–Co bond in **π-1-Co** but also reveal that the Co in **π-1-Co** is bonded with S and O, consistent with the results of FT-IR and XPS analyses. Quantitative EXAFS analysis (Fig. 2*D* and *SI Appendix*, Figs. S13 and S14) was carried out to investigate the structural parameters. Fitting the EXAFS curve, the numbers of S–Co and O–Co bonds in **π-1-Co** were determined to be 1.2 and 5.2, respectively, indicating that the Co is coordinated by one S, one carboxyl O, and four water O atoms (*SI Appendix*, Fig. S15 and Table S2). **π-1-M** have good chemical stability. After soaked in H_2O and general organic solvents, including methanol, acetonitrile, and toluene, for 12 h, the powder XRD patterns of **π-1-M** are similar to that of **π-1-M** freshly prepared (*SI Appendix*, Fig. S16), and the contents of M in **π-1-M** are also similar to those of **π-1-M** freshly prepared (Table S3). These observations illustrate that **π-1-M** possesses good stability in H_2O and general organic solvents.

Homogeneous Photocatalytic CO_2 Reduction. The homogeneous photocatalytic CO_2 reduction by $[Zn(phen)_2L]$ was conducted upon the irradiation by a 300 W Xe lamp in DMF, using triethanolamine (TEOA) as a sacrificial agent and Co(II), Fe(III), or Ni(II) as a cocatalyst. The result shows that, upon irradiation, the pure DMF would decompose to afford some amount of CO (*SI Appendix*, Fig. S17). What is important is that the equivalent amount of CO was detected in the presence of $[Zn(phen)_2L]$ or $CoCl_2/FeCl_3/NiCl_2$, indicating that $[Zn(phen)_2L]$ or $CoCl_2/FeCl_3/NiCl_2$ has no photocatalytic activity for conversion of CO_2 into CO, and they also would not boost the decomposition rate of DMF (*SI Appendix*, Fig. S18). However, in the DMF catalytic systems containing both $[Zn(phen)_2L]$ and $CoCl_2/FeCl_3$, the amount of CO generated obviously increases. These observations illustrate that $[Zn(phen)_2L]\&CoCl_2/FeCl_3$ possesses photocatalytic activity for CO_2 reduction to CO. As shown in *SI Appendix*, Fig. S19, the net amount of CO formed from CO_2 reduction by $[Zn(phen)_2L]\&CoCl_2$ and $[Zn(phen)_2L]\&FeCl_3$ are 0.98 and 0.15 µmol, respectively, while $[Zn(phen)_2L]\&NiCl_2$ exhibits almost no activity under the same conditions. Further control photocatalytic CO_2 reduction experiments were carried out for the DMF photocatalytic system containing $[Zn(phen)_2L]$, $CoCl_2$, and TEOA. It was found that, without $[Zn(phen)_2L]$, $CoCl_2$, TEOA, or light irradiation, no CO was detected (*SI Appendix*, Fig. S20), suggesting that all these conditions are indispensable for the photocatalytic reduction of CO_2 to CO.

During the process of photocatalytic CO_2 reduction by $[Zn(phen)_2L]\&CoCl_2$, it was found that the CO evolution rate slowed down significantly after 1 h, which may be related with the photodegradation of $[Zn(phen)_2L]$, as an obvious hypochromism of $[Zn(phen)_2L]$ DMF solution after irradiation for a certain time with an Xe lamp (*SI Appendix*, Fig. S2). This result indicates that mononuclear $[Zn(phen)_2L]$ complex in homogeneous DMF solution is prone to photodegradation. In addition, to reveal the photoinduced electron transfer process in the photocatalytic CO_2

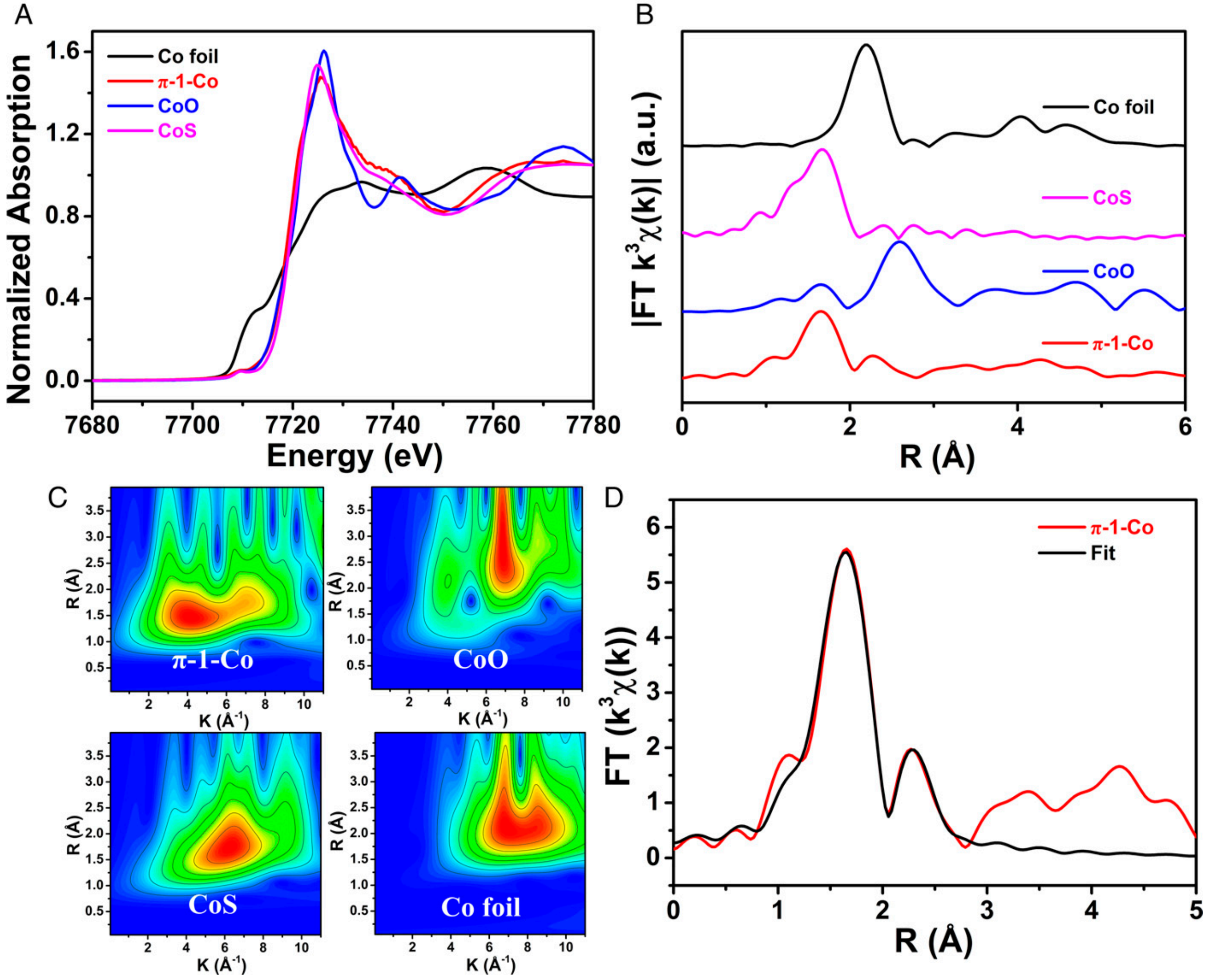

Fig. 2. (*A*) Co K-edge X-ray absorption near-edge structure spectra of **π-1-Co**, Co foil, CoO, and CoS. (*B*) EXAFS spectra of **π-1-Co**, Co foil, CoS, and CoO (a.u.: arbitrary unit). (*C*) Wavelet transform EXAFS of Co K-edge for **π-1-Co**, CoO, CoS, and Co foil. (*D*) The corresponding EXAFS R space–fitting result for **π-1-Co**.

reduction, the quenching mode of the [Zn(phen)$_2$L] in the excited state, [Zn(phen)$_2$L]*, was explored by titration of cocatalyst (CoCl$_2$) and electron donor (TEOA). As shown in *SI Appendix*, Fig. S21, [Zn(phen)$_2$L] in DMF shows strong fluorescence at 385 nm upon excitation at 330 nm. With the gradual addition of CoCl$_2$, the fluorescent intensity of [Zn(phen)$_2$L] dramatically decreased. In contrast, no obvious fluorescence intensity decrease was observed with the addition of TEOA. These observations illustrate that the quenched mode of the excited [Zn(phen)$_2$L]* can be assigned to an oxidatively quenched pathway, which means that the electron transfers from excited [Zn(phen)$_2$L]* to Co^{2+}. Based on these results, the reaction pathway for photocatalytic CO$_2$ reduction by [Zn(phen)$_2$L]&CoCl$_2$ can be proposed (Scheme 2). Upon illumination, [Zn(phen)$_2$L] adsorbs photons and is excited firstly. Then, the photogenerated electron of [Zn(phen)$_2$L]* transfers to the Co^{2+} center, generating Co species with lower valency. The positron in [Zn(phen)$_2$L]$^+$ is annihilated by TEOA and goes back to [Zn(phen)$_2$L]. The Co species with lower valency reduces the combined CO$_2$ to CO. After the release of CO, the catalytic system is regenerated, and the catalytic cycle restarts.

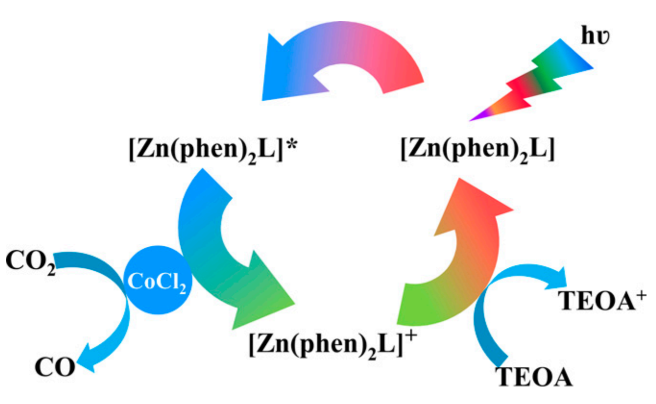

Scheme 2. Catalytic mechanism of [Zn(phen)$_2$L]&CoCl$_2$ for the visible, light-driven reduction of CO$_2$ to CO.

Heterogeneous Photocatalytic CO$_2$ Reduction. On the basis of the successful incorporation of M into **π-1**, as well as the excellent chemical stability of **π-1-M** in H$_2$O and common organic solvents, the photocatalytic CO$_2$ reduction experiments by **π-1-M** were performed in a CH$_3$CN/H$_2$O (4:1 in volume ratio) system. Other catalytic conditions are the same as those of homogeneous photocatalytic CO$_2$ reduction. As shown in

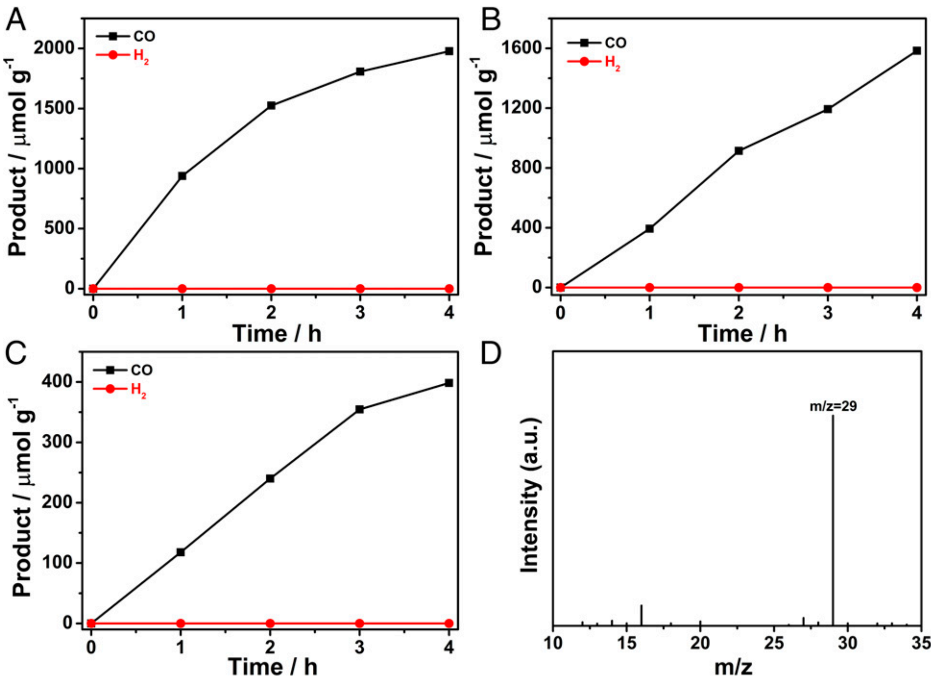

Fig. 3. Time-dependent photocatalytic evolution of CO and H_2 catalyzed by **π-1-Co** (*A*), **π-1-Fe** (*B*), and **π-1-Ni** (*C*). (*D*) Mass spectrum analyses for the generated gas from the photocatalytic reduction of $^{13}CO_2$ by **π-1-Co** (a.u.: arbitrary unit). Reaction conditions are the following: 2.0 mg catalyst, 5 mL CH_3CN/H_2O (4:1 in volume ratio), and 0.3 M TEOA on 300-W Xe lamp for 4 h at 25 °C.

Fig. 3, **π-1-M** show excellent activity and selectivity for photocatalytic CO_2 reduction to CO; no H_2 and hydrocarbon products such as CH_4 were generated (*SI Appendix*, Fig. S22), and no liquid product was detected in the reaction mixture either. Specifically, **π-1-Co** exhibits a CO production rate of 494.4 μmol · g^{-1} · h^{-1}, with a selectivity to CO of 100%. Under the same conditions, the CO production rates for **π-1-Fe** and **π-1-Ni** are 396.0 and 97.4 μmol · g^{-1} · h^{-1}, respectively (Table 1, Entries 1 to 3). The photocatalytic activity of **π-1-M** is dependent on the amount of M in **π-1-M**. When the concentration of metal–salt solution increases from 1 to 100 mM, the loading amount of M significantly increases (Table S1); the corresponding **π-1-M** also shows the best catalytic activity (*SI Appendix*, Fig. S23). Further increasing the concentration of metal–salt solution to 200 mM, the amount of M loaded in **π-1-M** is almost no change, and the amount of CO generated is also nearly unchanged. These results illustrate that the M amounts in **π-1-M** greatly affect the photocatalytic CO_2 activity. The M amount in **π-1-M**–induced, different catalytic activity can be attributed to different active sites. Remarkably, either for Co(II), Fe(III), or Ni(II), **π-1-M** in heterogeneous systems show greatly higher photocatalytic activity for CO_2 reduction than $[Zn(phen)_2L]$&M in homogeneous systems.

A series of control experiments with **π-1-Co** as a photocatalyst were performed to identify the key factors for CO_2-to-CO conversion. As shown in Table 1, without **π-1-Co**, TEOA, or illumination, no CO was generated in the catalytic system (Table 1, Entries 4 to 6). These results indicate that photocatalyst, sacrificial reductant, and light are all indispensable to photochemical CO_2-to-CO conversion. When using Ar instead of CO_2, no CO was detected either (Table 1, Entry 7), revealing that CO was generated from the reduction of CO_2, rather than

Table 1. The control experiments of heterogeneous photocatalytic CO_2 reduction*

Entry	Catalyst	CO (μmol · g^{-1} · h^{-1})	H_2 (μmol · g^{-1} · h^{-1})	CO (%)
1	**π-1-Co**	494.4	0	100
2	**π-1-Fe**	396.0	0	100
3	**π-1-Ni**	97.4	0	100
4†	—	0	0	—
5‡	**π-1-Co**	0	0	—
6§	**π-1-Co**	0	0	—
7¶	**π-1-Co**	0	0	—
8	**π-1**	0	0	—
9	H_2L&phen&Co(II)	20.0	0	100
10	H_2L&phen&Fe(III)	28.7	0	100
11	H_2L&phen&Ni(II)	8.7	0	100

*Reaction conditions : 2.0 mg catalyst, CH_3CN/H_2O (4:1 in volume ratio), 0.3 M TEOA, 300 W Xe lamp for 4 h at 25 °C.

†Without photocatalyst.

‡Without TEOA.

§Without light.

¶Ar atmosphere.

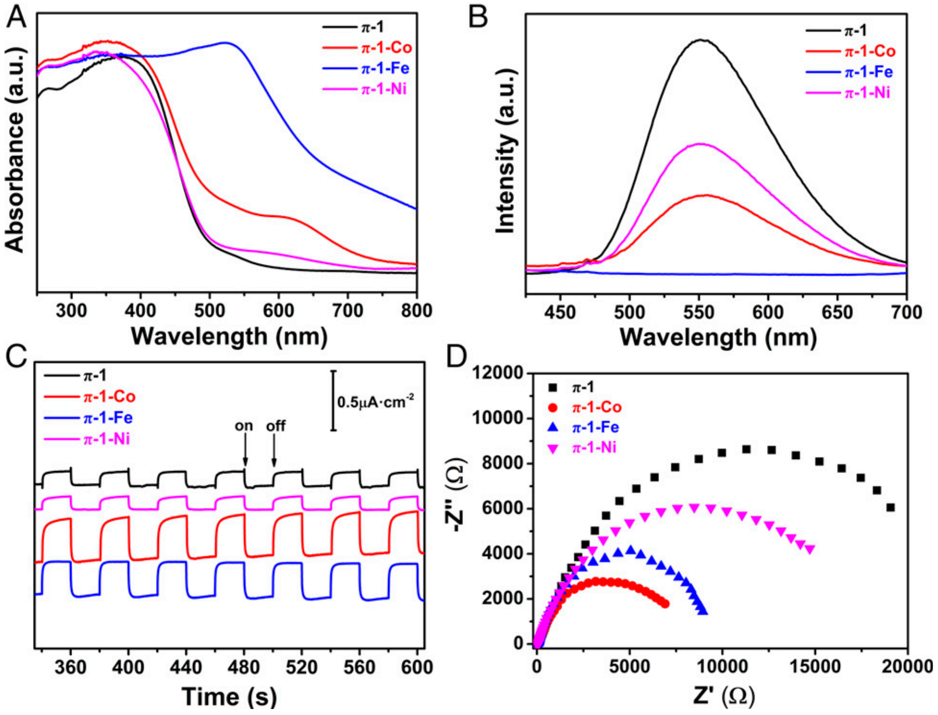

Fig. 4. UV-vis absorption spectra (*A*), PL spectra (*B*), photocurrent response (*C*), and Nyquist plots (*D*) of **π-1** and **π-1-M** (a.u.: arbitrary unit).

the decomposition of organic species in the photocatalytic system. This result was directly evidenced by isotope experiment, from which ^{13}CO was detected when using $^{13}CO_2$ instead of $^{12}CO_2$ under the same photocatalytic conditions (Fig. 3*D*). This solidly and directly evidences that the CO is originated from the photocatalytic CO_2 reduction. Then, we further carried out the photocatalytic reaction with **π-1** instead of **π-1-M**; no CO were detected, indicating that the anchored metal centers are the active sites and play significant role in photocatalytic CO_2 reduction (Table 1, Entry 8). We also performed the photocatalytic CO_2 reduction reaction by using a homogeneous mixture containing Zn(II), H_2L, phen, and Co(II)/Fe(III)/Ni(II). Only a negligible amount of CO was detected (Table 1, Entries 9 to 11). This result indicates that the order assembly of these constituents in a framework is also important for activity enhancement. Besides good activity, **π-1-Co** also possesses good durability. As shown in *SI Appendix*, Fig. S24, after three runs of photocatalytic CO_2 reduction reactions, only limited activity decrease was observed. SEM images reveal that the morphologies of **π-1-M** after photocatalytic reaction changes to microcrystals, which are similar to crushed **π-1** (*SI Appendix*, Fig. S25). Powder XRD and UV-vis absorption spectra measurements showed that the XRD patterns and UV-vis spectra of **π-1-M** after reaction are the same as before (*SI Appendix*, Figs. S26 and S27). All these observations suggest that **π-1-M** have good stability during the process of photocatalytic CO_2 reduction (47). It deserves to be mentioned that **π-1-M** exhibits better stability than [Zn(phen)$_2$L] in homogeneous solution, which may be attributed to the faster electron transfer of **π-1-M** in the heterogeneous system over [Zn(phen)$_2$L] in the homogeneous system. The fast electron transfer makes **π-1** avoid photocorrosion and photogradation.

Catalysis Mechanism. To reveal the enhanced photocatalytic performance of **π-1-M**, UV-vis absorption spectra, photoluminescence (PL) spectra, photocurrent response, and electrochemical impedance

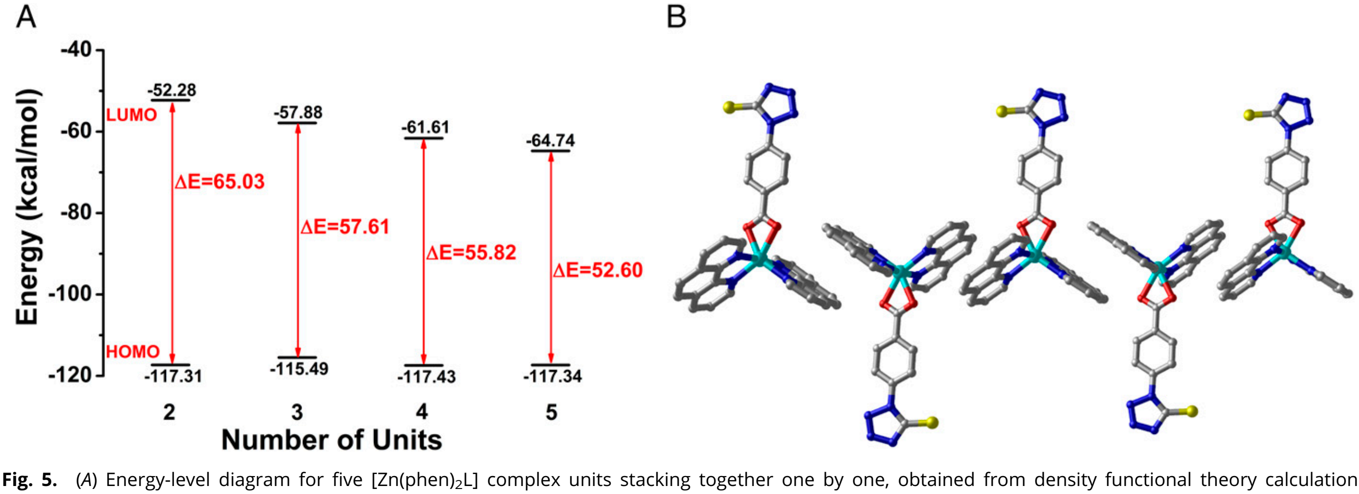

Fig. 5. (*A*) Energy-level diagram for five [Zn(phen)$_2$L] complex units stacking together one by one, obtained from density functional theory calculations (HOMO and LUMO). (*B*) Optimized structures for five [Zn(phen)$_2$L] complex units stacking together.

spectroscopy (EIS) of **π-1-M** and **π-1**, as a reference, were tested. It is clear to observe that the absorption band of **π-1** in the visible–light region remarkably strengthens after anchoring Co(II)/Fe(III)/Ni(II) (Fig. 4*A*), which means that electrons of **π-1-M** are more easily excited and transition upon light illumination than **π-1**. The PL spectra of **π-1-M**, especially for **π-1-Co** and **π-1-Fe**, show significantly damped emission in contrast to **π-1**, indicating that the recombination rate of the photogenerated charge carriers is enormously restrained (Fig. 4*B*). The photocurrent response tests showed that the current density of **π-1-M** is higher than that of **π-1**. Especially for **π-1-Co** and **π-1-Fe**, the current density are about three times higher than that of **π-1** (Fig. 4*C*). This suggests the better separation efficiency of photoinduced electrons in **π-1-M** over **π-1**. Transient fluorescence spectroscopy measurements demonstrated that the PL lifetime of **π-1** reduces from 22.56 to 11.33, 1.75, and 12.80 ns for **π-1-Co**, **π-1-Fe**, and **π-1-Ni**, respectively (*SI Appendix*, Fig. S28 and Table S4), further suggesting that the introduction of M significantly accelerates the electron transfer. EIS spectra show that the arc radius of **π-1-M** is much smaller than that of **π-1** (Fig. 4*D*), indicating that the charge transfer resistance of **π-1-M** is apparently lower than that of **π-1**. By UV-vis diffuse reflectance spectroscopy (DRS) and Mott−Schottky measurements, the band structures were examined. As shown in *SI Appendix*, Fig. S29, the band gaps for **π-1**, **π-1-Co**, **π-1-Fe**, and **π-1-Ni** were calculated to be 2.35, 2.17, 1.70, and 2.34 eV (versus normal hydrogen electrode [NHE]) by Tauc plots derived from the DRS, respectively. The flat band potentials (V_{fb}) for **π-1**, **π-1-Co**, **π-1-Fe**, and **π-1-Ni**, determined by Mott−Schottky measurements are −1.35, −1.26, −1.12, and −1.34 eV (versus NHE), respectively (*SI Appendix*, Fig. S30). It is generally known that the bottom of the conduction bands (CBs) in *n*-type semiconductors is more negative by −0.1 V than the V_{fb} (48–50). Thus, the corresponding CB edge potentials of **π-1**, **π-1-Co**, **π-1-Fe**, and **π-1-Ni** are −1.45, −1.36, −1.22, and −1.44 eV (versus NHE), respectively. Based on these CB edge potentials and the band gap positions, the valence band edge potentials of **π-1**, **π-1-Co**, **π-1-Fe**, and **π-1-Ni** were calculated to be 0.90, 0.81, 0.48, and 0.90 eV (versus NHE), respectively. Thus, the corresponding band structure diagram for **π-1**, **π-1-Co**, **π-1-Fe**, and **π-1-Ni** can be schemed and shown in *SI Appendix*, Fig. S31. Obviously, the CBs of **π-1-M** are more negative than the redox potentials of CO_2 to CO (−0.52 V versus NHE). Therefore, **π-1-M** could serve as effective photocatalysts to achieve photochemical CO_2 reduction to CO.

It is intriguing to find that the photocatalytic performance of mononuclear [Zn(phen)$_2$L] molecular photosensitizer could be greatly enhanced after order assembly via π–π stacking interactions. To demonstrate the change trend of photochemical and photophysical properties after ordered aggregation, the stacking energy and the highest occupied molecular orbital (HOMO)–lowest unoccupied molecular orbital (LUMO) energy gaps were calculated for five [Zn(phen)$_2$L] molecular photosensitizers stacking together one by one. As shown in Fig. 5 and *SI Appendix*, Fig. S32, with the number of [Zn(phen)$_2$L] increase from 2 to 3, 4, and 5, the stacking energy change from −33.63 to −59.05, −86.66, and −112.07 kcal/mol, indicating that more and more stable aggregation states were formed with the increase of [Zn(phen)$_2$L]. This result supports the experimental observation that, upon light irradiation, **π-1** shows good stability (*SI Appendix*, Fig. S33), while the mononuclear [Zn(phen)$_2$L] shows an obvious photodegradation (*SI Appendix*, Fig. S2). Moreover, with the increase of [Zn(phen)$_2$L] complex units, the energy gaps between HOMO and LUMO gradually decrease, indicating that the ordered aggregation of [Zn(phen)$_2$L] complex units is beneficial for electron transfer; thus, the photocatalytic activity can be remarkably enhanced.

Discussion

We evidenced herein a concept that highly crystalline heterogeneity of molecular photosensitizers could get ordered heterogeneous photocatalysts with enhanced photocatalytic activity. The obtained photocatalyst **π-1**, formed by connecting [Zn(phen)$_2$L] molecular photosensitizers merely through π–π stacking interactions, shows reduced energy gap over homogeneous [Zn(phen)$_2$L] and thus possesses noticeably better photocatalytic performance for CO_2 reduction than [Zn(phen)$_2$L] in the absence of additional photosensitizer. This work provides a strategy for designing crystalline-ordered heterogeneous photocatalysts with definite structures and enhanced, catalytic performance, which is still a great challenge in the development of heterogeneous photocatalysts.

Materials and Methods

All the chemicals were commercially available and used without further purification. FT-IR spectra were recorded on a PerkinElmer Frontier Mid-IR–FT-IR apparatus in attenuated total reflectance (ATR) or transmittance mode. Powder XRD measurements were carried out by using a Smart X-ray diffractometer (SmartLab 9 KW, Rigaku) with Cu Kα radiation (λ = 1.54178 Å). SEM images were acquired on an Environmental Scanning Electron Microscope with FEG (Quanta field emission gun [FEG] 250, FEI). XPS were recorded on an X-ray spectrometer (ESCALAB 250 Xi spectrometer, Thermo Fisher Scientific) with Al Kα as the excitation source. The contents of cobalt in **π-1-M** were quantified by an ICP-MS (NEXION300, PerkinElmer). The UV-vis DRS were obtained by a UV-vis spectrophotometer (UV-3600, Shimadzu). The product in gaseous phase of the reaction system was analyzed by gas chromatography (GC-2014+ATF, 230C, Shimadzu) equipped with thermal conductivity detector (TCD) and flame ionization detector (FID) dual detectors. The product in liquid phase of the reaction system was analyzed by an ion chromatograph (DX-600, Dionex). PL spectra were screened on a fluorescence spectrophotomer (F-7000, Hitachi). Time-resolved fluorescence spectra were tested by another fluorescence spectrophotomer (Horiba FL-3, HORIBA Scientific).

Data Availability. All study data are included in the article and/or *SI Appendix*.

ACKNOWLEDGMENTS. This work was supported by the National Key R&D Program of China (2017YFA0700104), the National Natural Science Foundation of China (22071182, 21861001, 21931007, and 21790052), the 111 Project of China (D17003), and the Science and Technology Development Fund of Tianjin Education Commission for Higher Education (2018KJ129).

Author affiliations: [a]Ministry of Education (MOE) International Joint Laboratory of Materials Microstructure, Institute for New Energy Materials and Low Carbon Technologies, School of Materials Science and Engineering, Tianjin University of Technology, Tianjin 300384, China

1. H. B. Gray, Powering the planet with solar fuel. *Nat. Chem.* **1**, 7 (2009).
2. Z. Wang, C. Li, K. Domen, Recent developments in heterogeneous photocatalysts for solar-driven overall water splitting. *Chem. Soc. Rev.* **48**, 2109–2125 (2019).
3. D.-C. Liu, D.-C. Zhong, T.-B. Lu, Non-noble metal-based molecular complexes for CO_2 reduction: From the ligand design perspective. *EnergyChem* **2**, 100034 (2020).
4. B. Sun *et al.*, Photoactive properties of supramolecular assembled short peptides. *Chem. Soc. Rev.* **48**, 4387–4400 (2019).
5. S. Wang *et al.*, Inside-and-out semiconductor engineering for CO_2 photoreduction: From recent advances to new trends. *Small Struct.* **2**, 2000061 (2021).
6. M. N. Chong, B. Jin, C. W. K. Chow, C. Saint, Recent developments in photocatalytic water treatment technology: A review. *Water Res.* **44**, 2997–3027 (2010).
7. Q. Wang, D. Astruc, State of the art and prospects in metal–organic framework (MOF)-based and MOF-derived nanocatalysis. *Chem. Rev.* **120**, 1438–1511 (2020).
8. H. Wang *et al.*, Semiconductor heterojunction photocatalysts: Design, construction, and photocatalytic performances. *Chem. Soc. Rev.* **43**, 5234–5244 (2014).
9. J.-H. Zhang *et al.*, Metal-organic layers as a platform for developing single-atom catalysts for photochemical CO_2 reduction. *Nano Energy* **80**, 105542 (2021).

10. Y.-N. Gong *et al.*, Regulating photocatalysis by spin-state manipulation of cobalt in covalent organic frameworks. *J. Am. Chem. Soc.* **142**, 16723–16731 (2020).
11. G. Wang *et al.*, Photoinduction of Cu single atoms decorated on UiO-66-NH_2 for enhanced photocatalytic reduction of CO_2 to liquid fuels. *J. Am. Chem. Soc.* **142**, 19339–19345 (2020).
12. X. Xiong *et al.*, Photocatalytic CO_2 reduction to CO over Ni single atoms supported on defect-rich zirconia. *Adv. Energy Mater.* **10**, 2002928 (2020).
13. X. Xiong *et al.*, Selective photocatalytic CO_2 reduction over Zn-based layered double hydroxides containing tri or tetravalent metals. *Sci. Bull.* **65**, 987–994 (2020).
14. H.-L. Wu, X.-B. Li, C.-H. Tung, L.-Z. Wu, Semiconductor quantum dots: An emerging candidate for CO_2 photoreduction. *Adv. Mater.* **31**, e1900709 (2019).
15. J. Wang *et al.*, β-cyclodextrin decorated CdS nanocrystals boosting the photocatalytic conversion of alcohols. *CCS Chem.* **2**, 81–88 (2020).
16. Y. Wang, X. Wang, M. Antonietti, Polymeric graphitic carbon nitride as a heterogeneous organocatalyst: From photochemistry to multipurpose catalysis to sustainable chemistry. *Angew. Chem. Int. Ed. Engl.* **51**, 68–89 (2012).
17. E. Boutin *et al.*, Molecular catalysis of CO_2 reduction: Recent advances and perspectives in electrochemical and light-driven processes with selected Fe, Ni and Co aza macrocyclic and polypyridine complexes. *Chem. Soc. Rev.* **49**, 5772–5809 (2020).
18. J.-W. Wang, D.-C. Zhong, T.-B. Lu, Artificial photosynthesis: Catalytic water oxidation and CO_2 reduction by dinuclear non-noble-metal molecular catalysts. *Coord. Chem. Rev.* **377**, 225–236 (2018).
19. D. Hong *et al.*, Efficient photocatalytic CO_2 reduction by a Ni(II) complex having pyridine pendants through capturing a Mg^{2+} ion as a Lewis-acid cocatalyst. *J. Am. Chem. Soc.* **141**, 20309–20317 (2019). Correction in: *J. Am. Chem. Soc.* **142**, 10229 (2020).
20. Z. Guo *et al.*, Selectivity control of CO versus $HCOO^-$ production in the visible-light-driven catalytic reduction of CO_2 with two cooperative metal sites. *Nat. Catal.* **2**, 801–808 (2019).
21. W. Nie, D. E. Tarnopol, C. C. L. McCrory, Enhancing a molecular electrocatalyst's activity for CO_2 reduction by simultaneously modulating three substituent effects. *J. Am. Chem. Soc.* **143**, 3764–3778 (2021).
22. H. Rao, L. C. Schmidt, J. Bonin, M. Robert, Visible-light-driven methane formation from CO_2 with a molecular iron catalyst. *Nature* **548**, 74–77 (2017).
23. A. Call *et al.*, Highly efficient and selective photocatalytic CO_2 reduction to CO in water by a cobalt porphyrin molecular catalyst. *ACS Catal.* **9**, 4867–4874 (2019).
24. B. Zhang, L. Sun, Artificial photosynthesis: Opportunities and challenges of molecular catalysts. *Chem. Soc. Rev.* **48**, 2216–2264 (2019).
25. Z. Guo *et al.*, Highly efficient and selective photocatalytic CO_2 reduction by iron and cobalt quaterpyridine complexes. *J. Am. Chem. Soc.* **138**, 9413–9416 (2016).
26. T. Ouyang, H.-H. Huang, J.-W. Wang, D.-C. Zhong, T.-B. Lu, A dinuclear cobalt cryptate as a homogeneous photocatalyst for highly selective and efficient visible-light driven CO_2 reduction to CO in CH_3CN/H_2O solution. *Angew. Chem. Int. Ed. Engl.* **56**, 738–743 (2017).
27. S. E. Lee *et al.*, Visible-light photocatalytic conversion of carbon dioxide by Ni(II) complexes with N_4S_2 coordination: Highly efficient and selective production of formate. *J. Am. Chem. Soc.* **142**, 19142–19149 (2020).
28. G. Zhao *et al.*, Co-porphyrin/carbon nitride hybrids for improved photocatalytic CO_2 reduction under visible light. *Appl. Catal. B* **200**, 141–149 (2017).
29. B. Ma *et al.*, Hybridization of molecular and graphene materials for CO_2 photocatalytic reduction with selectivity control. *J. Am. Chem. Soc.* **143**, 8414–8425 (2021).
30. S. Roy, E. Reisner, Visible-light-driven CO_2 reduction by mesoporous carbon nitride modified with polymeric cobalt phthalocyanine. *Angew. Chem. Int. Ed. Engl.* **58**, 12180–12184 (2019).
31. Q.-Q. Bi *et al.*, Selective photocatalytic CO_2 reduction in water by electrostatic assembly of CdS nanocrystals with a dinuclear cobalt catalyst. *ACS Catal.* **8**, 11815–11821 (2018).
32. Z. Pan *et al.*, Molecular junctions on polymeric carbon nitrides with enhanced photocatalytic performance. *ChemSusChem* **13**, 888–892 (2020).
33. R.-B. Lin *et al.*, Multifunctional porous hydrogen-bonded organic framework materials. *Chem. Soc. Rev.* **48**, 1362–1389 (2019).
34. B. Yu *et al.*, Robust biological hydrogen-bonded organic framework with post-functionalized rhenium(I) sites for efficient heterogeneous visible-light-driven CO_2 reduction. *Angew. Chem. Int. Ed. Engl.* **60**, 8983–8989 (2021).
35. Q. Yin *et al.*, An ultra-robust and crystalline redeemable hydrogen-bonded organic framework for synergistic chemo-photodynamic therapy. *Angew. Chem. Int. Ed. Engl.* **57**, 7691–7696 (2018).
36. X.-Z. Luo *et al.*, A microporous hydrogen-bonded organic framework: Exceptional stability and highly selective adsorption of gas and liquid. *J. Am. Chem. Soc.* **135**, 11684–11687 (2013).
37. I. Hisaki *et al.*, Acid responsive hydrogen-bonded organic frameworks. *J. Am. Chem. Soc.* **141**, 2111–2121 (2019).
38. J. H. Deng *et al.*, π-π stacking interactions: Non-negligible forces for stabilizing porous supramolecular frameworks. *Sci. Adv.* **6**, eaax9976 (2020).
39. G. B. Deacon, R. J. Phillips, Relationships between the carbon-oxygen stretching frequencies of carboxylato complexes and the type of carboxylate coordination. *Coord. Chem. Rev.* **33**, 227–250 (1980).
40. L.-P. Zhang, Y.-H. Wan, L.-P. Jin, Hydrothermal synthesis and crystal structure of neodymium(III) coordination polymers with isophthalic acid and 1,10-phenanthroline. *Polyhedron* **22**, 981–987 (2003).
41. C. W. Schlapfer, K. Nakamoto, Infrared spectra and normal-coordinate analysis of 1,2-dithiolate complexes with nickel. *Inorg. Chem.* **14**, 1338–1344 (1975).
42. H. Zhu *et al.*, When cubic cobalt sulfide meets layered molybdenum disulfide: A core-shell system toward synergetic electrocatalytic water splitting. *Adv. Mater.* **27**, 4752–4759 (2015).
43. W. Yang *et al.*, Tailoring crystal facets of metal–organic layers to enhance photocatalytic activity for CO_2 reduction. *Angew. Chem. Int. Ed. Engl.* **60**, 409–414 (2021).
44. L. Zhuang *et al.*, A surfactant-free and scalable general strategy for synthesizing ultrathin two-dimensional metal-organic framework nanosheets for the oxygen evolution reaction. *Angew. Chem. Int. Ed. Engl.* **58**, 13565–13572 (2019).
45. S. Zhang *et al.*, In situ embedding Co_9S_8 into nitrogen and sulfur codoped hollow porous carbon as a bifunctional electrocatalyst for oxygen reduction and hydrogen evolution reactions. *Appl. Catal. B* **254**, 186–193 (2019).
46. T. Yoon, K. S. Kim, One-step synthesis of CoS-doped β-$Co(OH)_2$@amorphous MoS_{2+x} hybrid catalyst grown on nickel foam for high-performance electrochemical overall water splitting. *Adv. Funct. Mater.* **26**, 7386–7393 (2016).
47. L.-Z. Dong *et al.*, Stable heterometallic cluster-based organic framework catalysts for artificial photosynthesis. *Angew. Chem. Int. Ed. Engl.* **59**, 2659–2663 (2020).
48. A. Ishikawa *et al.*, Oxysulfide $Sm_2Ti_2S_2O_5$ as a stable photocatalyst for water oxidation and reduction under visible light irradiation ($\lambda \leq 650$ nm). *J. Am. Chem. Soc.* **124**, 13547–13553 (2002).
49. H. Dong *et al.*, Regulation of metal ions in smart metal-cluster nodes of metal-organic frameworks with open metal sites for improved photocatalytic CO_2 reduction reaction. *Appl. Catal. B* **276**, 119173 (2020).
50. F.-M. Zhang *et al.*, Rational design of MOF/COF hybrid materials for photocatalytic H_2 evolution in the presence of sacrificial electron donors. *Angew. Chem. Int. Ed. Engl.* **57**, 12106–12110 (2018).